INTERNATIONAL JOURNAL FOR NUMERICAL METHODS IN FLUIDS, VOL. 19, 23–40 (1994)

MULTILEVEL METHODS FOR TEMPORAL AND SPATIAL FLOW TRANSITION SIMULATION IN A ROUGH CHANNEL*

ZHINING LIU, ZHIXING LIU, CHAOQUN LIU AND STEVE MCCORMICK

Department of Mathematics, University of Colorado at Denver, Campus Box 170, PO Box 173364, Denver, CO 80217-3364, U.S.A.

SUMMARY

We investigate the instability of 2D incompressible flows in a rough planar channel by tracking the growth of the unstable mode in its early stage. We develop both second- and fourth-order finite difference methods on a staggered grid, together with a fully implicit time-marching scheme, using grid generation to accommodate fairly general geometries. A multigrid full approximation scheme based on the line-distributive relaxation method is used for fast convergence. For a 2D smooth channel, numerical results show good agreement with the analytic solution obtained from linear theory for small disturbances. Numerical results for a 2D channel with one and two roughness elements are analysed by Fourier analysis. They show how the roughness elements affect the growth of the perturbation.

KEY WORDS Flow transition General geometry Multigrid Roughness

1. INTRODUCTION

Developing an understanding of flow transition at high Reynolds numbers has been a central problem in the theory of fluid motion for over a century. It also has great practical interest. Numerical simulation of flow transition in a channel has been successfully accomplished by several researchers,[1,2] most of whom use spectral methods with explicit time marching and non-staggered grids.[3] A computationally efficient 'temporal' approach[4] which follows the time evolution of a single wavelength of the disturbance has been widely applied to simulate the transition process. A very efficient multigrid finite volume scheme developed by Liu *et al.*[5–7] achieves very good agreement with linear theory for temporal evolution induced by small disturbances, but the computation was performed only on uniform grids. In order to obtain more accurate results, we must use a rather fine grid for adequate resolution of the boundary layers where the velocity of the flow has large gradients. For this reason, here we use a transformation to change our problem from physical to computational co-ordinates. In the computational plane the grid is uniform, although the corresponding grid is generally non-uniform in the physical plane. For example, we can make the mesh finer near solid walls but coarser elsewhere. In this way the governing equations may be solved on a uniform grid using a rather standard multigrid method.

In this paper we first derive the governing Navier–Stokes equations in the computational plane in such a way that the continuity equation maintains the same conservation form as in

* Selected paper from the 'BAIL VI Conference, Colorado, U.S.A. 1992'-Special Editor: Professor J.H.H. Miller.

CCC 0271–2091/94/130019–18

Received January 1993
Revised January 1994

the physical plane. This makes it easy to apply the distributive relaxation scheme. The discretization is then accomplished by finite differences on a staggered grid in space, with second-order backward Euler in time. We use multigrid for fast solution of the large linear system arising at each time step. Flow transition in a planar channel is employed as a model problem and as a basis for assessing the accuracy and efficiency of our approach.

The more realistic spatial approach, which concerns not only the single wavelength of the flow but several wavelengths, is also employed in this paper. A multidomain method[8] is applied here to avoid possible reflection of the outgoing wave from the outflow boundary. At $Re = 5000$, which corresponds to a decreasing mode according to linear stability theory, we use both single and double solitary-type roughness elements to investigate the influence of roughness on transition. A Fourier transformation is then used to analyse the increasing rate of different Fourier modes of the disturbance; it clearly shows that roughness makes the flow more unstable by inducing high-frequency waves.

2. GOVERNING EQUATIONS AND BOUNDARY CONDITIONS

The two-dimensional, time-dependent, incompressible Navier–Stokes equations are used as the governing equations for the planar channel flow:

$$\frac{\partial u}{\partial t} + \frac{\partial uu}{\partial x} + \frac{\partial uv}{\partial y} - \frac{1}{Re}\left(\frac{\partial^2 u}{\partial x^2} + \frac{\partial^2 u}{\partial y^2}\right) + \frac{\partial p}{\partial x} = 0, \tag{1}$$

$$\frac{\partial v}{\partial t} + \frac{\partial uv}{\partial x} + \frac{\partial vv}{\partial y} - \frac{1}{Re}\left(\frac{\partial^2 v}{\partial x^2} + \frac{\partial^2 v}{\partial y^2}\right) + \frac{\partial p}{\partial y} = 0, \tag{2}$$

$$\frac{\partial u}{\partial x} + \frac{\partial v}{\partial y} = 0, \tag{3}$$

where u and v are the velocity components in the x- and y-directions respectively and p is the pressure. The equations are non-dimensionalized with respect to the centreline velocity U_0, channel half-width h, kinematic viscosity parameter ν, and Reynolds number

$$Re = U_0 h/\nu. \tag{4}$$

The computational domain in the y-direction is now restricted to $y \in [0, 2]$. The boundary conditions on the solid walls are (see Figure 1)

$$u(x, 0, t) = v(x, 0, t) = 0, \qquad u(x, 2, t) = v(x, 2, t) = 0. \tag{5}$$

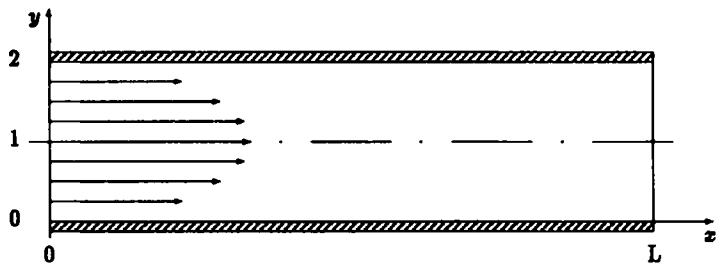

Figure 1. Planar channel flow

Because we use a staggered grid, boundary conditions for p are not needed on the solid wall. For simplicity we consider the temporal instability first for channel flows and assume periodic boundary conditions in the x- direction:

$$u(x, y, t) = u(x + L, y, t), \qquad v(x, y, t) = v(x + L, y, t), \qquad p(x, y, t) = p(x + L, y, t) + \frac{2}{Re} L, \tag{6}$$

where L is the wavelength of a specified mode of disturbance.

Poiseuille flow is the steady state solution of (1)–(3), whose variables are denoted by u_0, v_0 and p_0:

$$u_0(x, y, t) = 1 - (y - 1)^2, \qquad v_0(x, y, t) = 0, \qquad p_0(x, y, t) = -\frac{2}{Re} x + C. \tag{7}$$

Here C is a constant. This solution is used as the undisturbed base solution.

If we impose some disturbance at $t = 0$ on Poiseuille flow, it will generally become time-dependent. For such a disturbed flow, in order to reduce round-off error in the computational procedure, we write the primitive variables in the perturbation form

$$u = u_0 + u', \qquad v = v_0 + v', \qquad p = p_0 + p'. \tag{8}$$

Substituting (8) into (1)–(3), using the fact that $v_0 = 0$ and eliminating the terms for the steady base flow, we may then rewrite the governing equations in the perturbation form

$$\frac{\partial u}{\partial t} + \frac{\partial u_0 u}{\partial x} + v\frac{\partial u_0}{\partial y} + \frac{\partial uu}{\partial x} + \frac{\partial uv}{\partial y} - \frac{1}{Re}\left(\frac{\partial^2 u}{\partial x^2} + \frac{\partial^2 u}{\partial y^2}\right) + \frac{\partial p}{\partial x} = 0, \tag{9}$$

$$\frac{\partial v}{\partial t} + \frac{\partial u_0 v}{\partial x} + \frac{\partial uv}{\partial x} + \frac{\partial vv}{\partial y} - \frac{1}{Re}\left(\frac{\partial^2 v}{\partial x^2} + \frac{\partial^2 v}{\partial y^2}\right) + \frac{\partial p}{\partial y} = 0, \tag{10}$$

$$\frac{\partial u}{\partial x} + \frac{\partial v}{\partial y} = 0. \tag{11}$$

Here for simplicity we drop the prime notation so that u, v and p now actually stand for the perturbation variables u', v' and p'. Note that the driving term $-2/Re$ has been eliminated from (9) by the steady base flow equivalent. The boundary conditions may now be rewritten as

$$u(x, 0, t) = v(x, 0, t) = 0, \qquad u(x, 2, t) = v(x, 2, t) = 0,$$

$$u(x, y, t) = u(x + L, y, t), \qquad v(x, y, t) = v(x + L, y, t),$$

$$p(x, y, t) = p(x + L, y, t). \tag{12}$$

3. PERTURBATION FORM IN THE COMPUTATIONAL PLANE

To meet the requirements of general geometry, a one-to-one mapping is used to transfer an arbitrary domain in the physical plane to the computational plane. In Figure 2, Ω represents an arbitrary domain in the Cartesian co-ordinate system, and AB, BC, CD and DA are its smooth

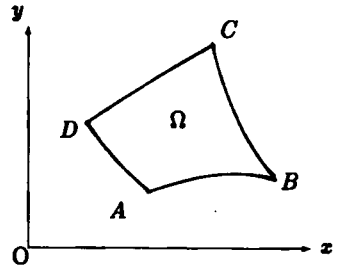

Figure 2. Physical plane

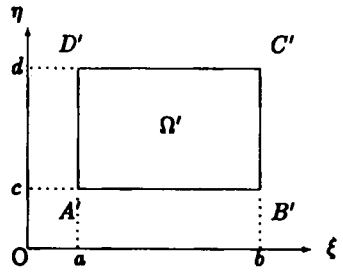

Figure 3. Computational plane

boundary segments. The objective is to solve problem (9)–(12) on the domain Ω, which we will map on to the computational domain Ω′ depicted in Figure 3.

Assume that there exists an one-to-one co-ordinate transformation

$$x = x(\xi, \eta), \qquad y = y(\xi, \eta) \tag{13}$$

from the computational plane (ξ, η) to the physical plane (x, y) and that the domain Ω′ in the plane (ξ, η) is a rectangular region. Here we assume that $x(\xi, \eta)$ and $y(\xi, \eta)$ are smooth functions on Ω′ and that the transformation is one-to-one, so we have

$$J = \begin{vmatrix} x_\xi & y_\xi \\ x_\eta & y_\eta \end{vmatrix} = x_\xi y_\eta - x_\eta y_\xi \neq 0. \tag{14}$$

J is the Jacobian of the co-ordinate transformation (13). We then obtain the relations

$$\xi_x = y_\eta/J, \qquad \eta_x = -y_\xi/J, \qquad \xi_y = -x_\eta/J, \qquad \eta_y = x_\xi/J. \tag{15}$$

To derive the representation of equations (9)–(11) in the plane (ξ, η), we suppose ϕ is a generic differentiable function in the plane (x, y). Thus

$$\frac{\partial \phi}{\partial x} = \phi_\xi \xi_x + \phi_\eta \eta_x = \frac{1}{J}(\phi_\xi y_\eta - \phi_\eta y_\xi) = \frac{1}{J}[(y_\eta \phi)_\xi - (y_\xi \phi)_\eta], \tag{16}$$

$$\frac{\partial \phi}{\partial y} = \phi_\xi \xi_y + \phi_\eta \eta_y = \frac{1}{J}(-\phi_\xi x_\eta + \phi_\eta x_\xi) = \frac{1}{J}[(-x_\eta \phi)_\xi + (x_\xi \phi)_\eta]. \tag{17}$$

Using these formulae, we obtain the following system of equations in the new variables U, V and p:

$$\frac{\partial(x_\xi U + x_\eta V)}{\partial t} + u_0\left[\frac{\partial}{\partial\xi}\left(\frac{y_\eta}{J}(x_\xi U + x_\eta V)\right) + \frac{\partial}{\partial\eta}\left(\frac{y_\xi}{J}(x_\xi U + x_\eta V)\right)\right] + \frac{\partial}{\partial\xi}\left(\frac{1}{J}(x_\xi U + x_\eta V)U\right)$$
$$+ \frac{\partial}{\partial\eta}\left(\frac{1}{J}(x_\xi U + x_\eta V)V\right) - \frac{1}{Re}\frac{\partial}{\partial\xi}\left[\frac{\alpha}{J}\frac{\partial}{\partial\xi}\left(\frac{1}{J}(x_\xi U + x_\eta V)\right)\right.$$
$$\left. - \frac{\beta}{J}\frac{\partial}{\partial\eta}\left(\frac{1}{J}(x_\xi U + x_\eta V)\right)\right] - \frac{1}{Re}\frac{\partial}{\partial\eta}\left[-\frac{\beta}{J}\frac{\partial}{\partial\xi}\left(\frac{1}{J}(x_\xi U + x_\eta V)\right)\right.$$
$$\left. + \frac{\gamma}{J}\frac{\partial}{\partial\eta}\left(\frac{1}{J}(x_\xi U + x_\eta V)\right)\right]$$
$$+ \frac{\partial(y_\eta p)}{\partial\xi} - \frac{\partial(y_\xi p)}{\partial\eta} - 2(y-1)(y_\xi U + y_\eta V) = 0, \tag{18}$$

$$\frac{\partial(y_\xi U + y_\eta V)}{\partial t} + u_0\left[\frac{\partial}{\partial\xi}\left(\frac{y_\eta}{J}(y_\xi U + y_\eta V)\right) - \frac{\partial}{\partial\eta}\left(\frac{y_\xi}{J}(y_\xi U + y_\eta V)\right)\right] + \frac{\partial}{\partial\xi}\left(\frac{1}{J}(y_\xi U + y_\eta V)U\right)$$
$$+ \frac{\partial}{\partial\eta}\left(\frac{1}{J}(y_\xi U + y_\eta V)V\right) - \frac{1}{Re}\frac{\partial}{\partial\xi}\left[\frac{\alpha}{J}\frac{\partial}{\partial\xi}\left(\frac{1}{J}(y_\xi U + y_\eta V)\right)\right.$$
$$\left. - \frac{\beta}{J}\frac{\partial}{\partial\eta}\left(\frac{1}{J}(y_\xi U + y_\eta V)\right)\right] - \frac{1}{Re}\frac{\partial}{\partial\eta}\left[-\frac{\beta}{J}\frac{\partial}{\partial\xi}\left(\frac{1}{J}(y_\xi U + y_\eta V)\right)\right.$$
$$\left. + \frac{\gamma}{J}\frac{\partial}{\partial\eta}\left(\frac{1}{J}(y_\xi U + y_\eta V)\right)\right]$$
$$- \frac{\partial(x_\eta p)}{\partial\xi} + \frac{\partial(x_\xi p)}{\partial\eta} = 0, \tag{19}$$

$$\frac{\partial U}{\partial\xi} + \frac{\partial V}{\partial\eta} = 0. \tag{20}$$

Here

$$U = y_\eta u - x_\eta v, \qquad v = x_\xi v - y_\xi u,$$
$$\alpha = x_\eta^2 + y_\eta^2, \qquad \beta = x_\xi x_\eta + y_\xi y_\eta, \qquad \gamma = x_\xi^2 + y_\xi^2.$$

Note that the computational continuity equation (20) is of the same form as the physical one (11).

Equations (18)–(20) are equations (9)–(11) transformed to the computational plane (ξ, η). Thus, instead of solving (9)–(11), we can solve (18)–(20) and recover the original velocities by

$$u = \frac{1}{J}(x_\xi U + x_\eta V), \tag{21}$$

$$v = \frac{1}{J}(y_\xi U + y_\eta V). \tag{22}$$

The boundary conditions on the solid walls become (see Figure 3)

$$U(\xi, c, t) = V(\xi, c, t) = 0, \qquad U(\xi, d, t) = V(\xi, d, t) = 0 \tag{23}$$

and the periodic boundary conditions in the ξ-direction are

$$U(\xi, \eta, t) = U(\xi + l, \eta, t), \qquad V(\xi, \eta, t) = V(\xi + l, \eta, t), \qquad p(\xi, \eta, t) = p(\xi + l, \eta, t), \tag{24}$$

where $l = b - a$. For convenience we will call (18)–(20) the U-equation, the V-equation and the continuity equation respectively.

4. SECOND-ORDER FULLY IMPLICIT SCHEME

In the computational plane we use a uniform staggered grid for the discretization (see Figure 4). Horizontal arrows represent locations where U-values are assigned, vertical arrows V-values and circles p-values. Although both second- and fourth-order schemes are developed, for simplicity of discussion we will focus only on the second-order scheme. Our indexing scheme is indicated in Figure 4, with a typical neighbourhood depicted in Figure 5.

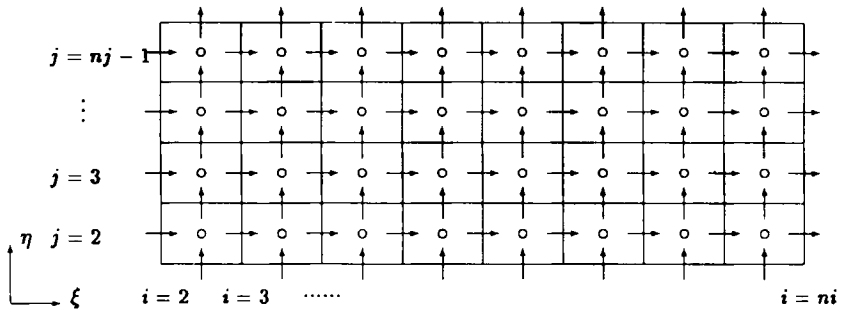

Figure 4. Staggered grid in computational plane (ξ, η). Indices for U-points are noted

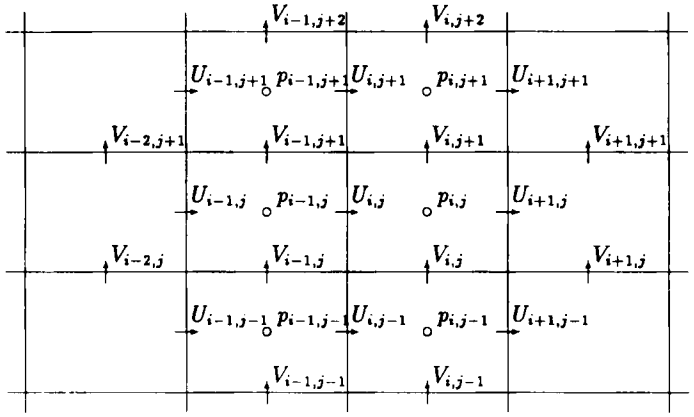

Figure 5. Subscript systems for U- V- and p-points

We will refer to values of the velocities at points other than their prime location. Such values will be denoted by an overbar and will invariably reference indices of the opposing velocity. For example, we will use $\bar{V}_{i,j}$ to represent the value of V at the point (i,j) which is based on the U-subscript system. Similarly $\bar{U}_{i,j}$ represents the value of U at the point (i,j) which is based on the V-subscript system. We use second-order interpolation to obtain the averages

$$\bar{U}_{i,j} = \tfrac{1}{4}(U_{i,j-1} + U_{i+1,j-1} + U_{i,j} + U_{i+1,j}), \qquad \bar{V}_{i,j} = \tfrac{1}{4}(V_{i-1,j} + V_{i,j} + V_{i-1,j+1} + V_{i,j+1}).$$

4.1. Discretization

A second-order backward Euler in time and a second-order finite difference in space are applied to discretize equations (18)–(20). Since these equations are quite complicated, we do not detail the full discretization here, but instead describe the discretization form for several of its terms.

First, the time derivative terms of (18) are discretized as illustrated by the following (here all indices refer to the U-subscript system):

$$\left(x_\xi \frac{\partial U}{\partial t} + x_\eta \frac{\partial V}{\partial t}\right)_{i,j} = \frac{x_{\xi_{i,j}}}{2\Delta t}(3U_{i,j}^{n+1} - 4U_{i,j}^{n} + U_{i,j}^{n-1}) + \frac{x_{\eta_{i,j}}}{2\Delta t}(3\bar{V}_{i,j}^{n+1} - 4\bar{V}_{i,j}^{n} + \bar{V}_{i,j}^{n-1}), \quad (25)$$

where superscripts n and $n-1$ signify earlier time levels, and the current time level, signified by $n+1$, is otherwise assumed.

Other terms in (18) are discretized as follows (here we use index offsets of $\frac{1}{2}$ in intermediate expressions to suggest the averaging formulae we develop):

$$\begin{aligned}
&\left[\frac{\partial}{\partial \eta}\left(\frac{1}{J}(x_\xi U + x_\eta V)V\right)\right]_{i,j} \\
&\quad = \frac{1}{\Delta\eta}\left[\frac{1}{J_{i,j+1/2}}\left(x_{\xi_{i,j+1/2}}\frac{U_{i,j}+U_{i,j+1}}{2} + x_{\eta_{i,j+1/2}}\frac{V_{i-1,j+1}+V_{i,j+1}}{2}\right)\frac{V_{i-1,j+1}+V_{i,j+1}}{2}\right. \\
&\qquad \left. - \frac{1}{J_{i,j-1/2}}\left(x_{\xi_{i,j-1/2}}\frac{U_{i,j-1}+U_{i,j}}{2} + x_{\eta_{i,j-1/2}}\frac{V_{i-1,j}+V_{i,j}}{2}\right)\frac{V_{i-1,j}+V_{i,j}}{2}\right], \qquad (26)
\end{aligned}$$

$$\begin{aligned}
&\left\{-\frac{1}{Re}\frac{\partial}{\partial\eta}\left[\frac{\gamma}{J}\frac{\partial}{\partial\eta}\left(\frac{1}{J}(x_\xi U + x_\eta V)\right)\right]\right\}_{i,j} \\
&\quad = -\frac{1}{Re}\frac{1}{\Delta\eta}\left\{\frac{\gamma_{i,j+1/2}}{J_{i,j+1/2}}\frac{1}{\Delta\eta}\left[\left(\frac{1}{J}(x_\xi U + x_\eta \bar{V})\right)_{i,j+1} - \left(\frac{1}{J}(x_\xi U + x_\eta \bar{V})\right)_{i,j}\right]\right. \\
&\qquad \left. - \frac{\gamma_{i,j-1/2}}{J_{i,j-1/2}}\frac{1}{\Delta\eta}\left[\left(\frac{1}{J}(x_\xi U + x_\eta \bar{V})\right)_{i,j} - \left(\frac{1}{J}(x_\xi U + x_\eta \bar{V})\right)_{i,j-1}\right]\right\}, \qquad (27)
\end{aligned}$$

$$\begin{aligned}
&\left(\frac{\partial(y_\eta p)}{\partial\xi} - \frac{\partial(y_\xi p)}{\partial\eta}\right)_{i,j} \\
&\quad = \frac{1}{\Delta\xi}(y_{\eta_{i+1/2,j}}p_{i,j} - y_{\eta_{i-1/2,j}}p_{i-1,j}) - \frac{1}{\Delta\eta}\left(y_{\xi_{i,j+1/2}}\frac{p_{i-1,j}+p_{i,j}+p_{i-1,j+1}+p_{i,j+1}}{4}\right. \\
&\qquad \left. - y_{\xi_{i,j-1/2}}\frac{p_{i-1,j-1}+p_{i,j-1}+p_{i-1,j}+p_{i,j}}{4}\right). \qquad (28)
\end{aligned}$$

The continuity equation is very simple to discretize:

$$\frac{1}{\Delta\xi}(U_{i+1,j} - U_{ij}) + \frac{1}{\Delta\eta}(V_{i,j+1} - V_{i,j}) = 0. \tag{29}$$

4.2. General form of the finite difference equations

At every point (i, j) of the U-system, V-system or p-system respectively the finite difference scheme for equations (18)–(20) can be written in a general form as

$$AN_{i,j}U_{i,j+1} + AS_{i,j}U_{i,j-1} + AE_{i,j}U_{i+1,j} + AW_{i,j}U_{i-1,j} + AC_{i,j}U_{i,j} + APC_{i,j}p_{i,j} + APW_{i,j}p_{i-1,j} + X_{i,j} = R_{i,j}, \tag{30}$$

$$BN_{i,j}V_{i,j+1} + BS_{i,j}V_{i,j-1} + BE_{i,j}V_{i+1,j} + BW_{i,j}V_{i-1,j} + BC_{i,j}V_{i,j} + BPC_{i,j}p_{i,j} + BPS_{i,j}p_{i,j-1} + Y_{i,j} = S_{i,j}, \tag{31}$$

$$CUE_{i,j}U_{i+1,j} + CUC_{i,j}U_{i,j} + CVN_{i,j}V_{i,j+1} + CVC_{i,j}V_{i,j-1} = T_{i,j}. \tag{32}$$

Here, taking the U-equation as an example, AE, AW, AN, AS and AC are the coefficients for the discretized U-points. APC and APW are the coefficients for the discretized p-points, R is the source term, which does not change during the given time step, and X includes other terms and must be updated after each iteration, but is frozen during each relaxation sweep.

The coefficients of equations (30)–(32) are quite complicated, so we do not express them in detail here.

4.3. Boundary modification

In the ξ-direction we have the periodic boundary conditions

$$U_{1,j} = U_{ni-1,j}, \qquad V_{1,j} = V_{ni-1,j}, \qquad p_{1,j} = p_{ni-1,j},$$
$$U_{ni,j} = U_{2,j}, \qquad V_{ni,j} = V_{2,j}, \qquad p_{ni,j} = p_{2,j},$$

where ni is the number of grid points in the ξ-direction.

At the solid wall boundary some of the formulae used in Section 4.1 are inappropriate. We modify them as follows.

First consider the U-equation for $j = 2$ (see Figure 6). In (27) the computational formula for

$$\left[\frac{\gamma}{J}\frac{\partial}{\partial\eta}\left(\frac{1}{J}(x_\xi U + x_\eta V)\right)\right]_{i,j-1/2}$$

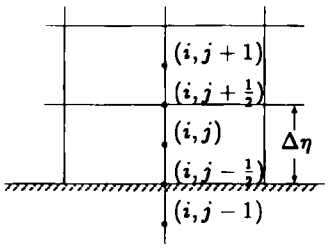

Figure 6. Bottom solid wall

is inappropriate because it needs the value

$$\left(\frac{1}{J}(x_\xi U + x_\eta \bar{V})\right)_{i,j-1},$$

which references the point $(i, j-1)$ outside the computational domain. To avoid using the ghost points, we derive the formula directly. For a generic function ϕ a Taylor series expansion yields

$$\phi_{\eta_{i,j-1/2}} = \frac{1}{3\Delta\eta}(9\phi_{i,j} - \phi_{i,j+1} - 8\phi_{i,j-1/2}) + O(\Delta\eta^2). \tag{33}$$

Note that both U and V are zero at the solid wall, so we have

$$\left[\frac{\partial}{\partial\eta}\left(\frac{1}{J}(x_\xi U + x_\eta V)\right)\right]_{i,j-1/2} = \frac{1}{3\Delta\eta}\left[9\left(\frac{1}{J}(x_\xi U + x_\eta \bar{V})\right)_{i,j} - \left(\frac{1}{J}(x_\xi U + x_\eta \bar{V})\right)_{i,j+1}\right].$$

For (28) we use the analogous expansion

$$\phi_{\eta_{i,j}} = \frac{1}{\Delta\eta}(-3\phi_{i,j} + 4\phi_{i,j+1/2} - \phi_{i,j+1}) + O(\Delta\eta^2) \tag{34}$$

to derive the term

$$-\left(\frac{\partial(y_\xi p)}{\partial\eta}\right)_{i,j} = \frac{1}{\Delta\eta}\left(3y_{\xi_{i,j}}\frac{p_{i-1,j}+p_{i,j}}{2} - y_{\xi_{i,j+1/2}}(p_{i-1,j} + p_{i,j} + p_{i,j+1} + p_{i,j+1}) + y_{\xi_{i,j+1}}\frac{p_{i-1,j+1}+p_{i,j+1}}{2}\right).$$

To be more specific, the modified formulae for the U-equation at $j = 2$ are as follows (superscript '*old*' refers to the unmodified formulae, '*new*' to the modified ones):

$$AC_{i,j}^{\text{new}} = AC_{i,j}^{\text{old}} + \frac{x_{\xi_{i,j-1/2}}}{4\Delta\eta J_{i,j-1/2}}(V_{i-1,j} + V_{i,j})$$
$$+ \frac{1}{4Re\Delta\xi\Delta\eta}\left(\frac{\beta_{i+1/2,j}x_{\xi_{i+1/2,j-1/2}}}{J_{i+1/2,j}J_{i+1/2,j-1/2}} - \frac{\beta_{i-1/2,j}x_{\xi_{i-1/2,j-1/2}}}{J_{i-1/2,j}J_{i-1/2,j-1/2}}\right)$$
$$+ \frac{1}{4Re\Delta\xi\Delta\eta}\frac{\beta_{i,j-1/2}}{J_{i,j-1/2}}\left(\frac{x_{\xi_{i+1/2,j-1/2}}}{J_{i+1/2,j-1/2}} - \frac{x_{\xi_{i-1/2,j-1/2}}}{J_{i-1/2,j-1/2}}\right) + \frac{2}{Re\Delta\eta^2}\frac{\gamma_{i,j-1/2}x_{\xi_{i,j}}}{J_{i,j-1/2}J_{i,j}}$$

$$AE_{i,j}^{\text{new}} = AE_{i,j}^{\text{old}} + \frac{1}{4Re\Delta\xi\Delta\eta}\frac{x_{\xi_{i+1/2,j-1/2}}}{J_{i+1/2,j-1/2}}\left(\frac{\beta_{i+1/2,j}}{J_{i+1/2,j}} + \frac{\beta_{i,j-1/2}}{J_{i,j-1/2}}\right),$$

$$AW_{i,j}^{\text{new}} = AW_{i,j}^{\text{old}} - \frac{1}{4Re\Delta\xi\Delta\eta}\frac{x_{\xi_{i-1/2,j-1/2}}}{J_{i-1/2,j-1/2}}\left(\frac{\beta_{i-1/2,j}}{J_{i-1/2,j}} + \frac{\beta_{i,j-1/2}}{J_{i,j-1/2}}\right),$$

$$AN_{i,j}^{\text{new}} = AN_{i,j}^{\text{old}} - \frac{1}{3Re\Delta\eta^2}\frac{\gamma_{i,j-1/2}x_{\xi_{i,j+1}}}{J_{i,j-1/2}J_{i,j+1}},$$

$$AS_{i,j}^{\text{new}} = 0,$$

$$APC_{i,j}^{\text{new}} = APC_{i,j}^{\text{old}} + \frac{1}{2\Delta\eta}(3y_{\xi_{i,j}} - 2y_{\xi_{i,j+1/2}}) - \frac{1}{4\Delta\eta}(y_{\xi_{i,j-1/2}} - y_{\xi_{i,j+1/2}}),$$

$$APW_{i,j}^{\text{new}} = APW_{i,j}^{\text{old}} + \frac{1}{2\Delta\eta}(3y_{\xi_{i,j}} - 2y_{\xi_{i,j+1/2}}) - \frac{1}{4\Delta\eta}(y_{\xi_{i,j-1/2}} - y_{\xi_{i,j+1/2}}).$$

Modifications for the U-equation at $j = nj - 1$ and for the V-equation at $j = 2$ and $nj - 1$ are analogous.

5. DISTRIBUTIVE RELAXATION AND MULTIGRID

At each time step we need to solve the spatial system (30)–(32). For this purpose we have developed an efficient multigrid scheme based on a distributive relaxation, which is described loosely as follows.[9]

First apply the line Gauss–Seidel relaxation to update U in (30) and V in (31). Then for each box based on $p_{i,j}$ we adjust $U_{i,j}$, $U_{i+1,j}$, $V_{i,j}$, $V_{i,j+1}$ and $p_{i,j}$ simultaneously to satisfy the associated neighbouring four momentum equations and continuity equation, using the corrections given in the form (see Figure 7)

$$U_{i,j}^{\text{new}} = U_{i,j} - \delta U_{i,j}, \qquad U_{i+1,j}^{\text{new}} = U_{i+1,j} + \delta U_{i,j},$$

$$V_{i,j}^{\text{new}} = V_{i,j} - \delta V_{i,j}, \qquad V_{i,j+1}^{\text{new}} = V_{i,j+1} + \delta V_{i,j},$$

$$p_{i,j}^{\text{new}} = p_{i,j} + \delta p_{i,j}.$$

The corresponding equations for these corrections are

$$(AE_{i,j} - AC_{i,j})\delta U_{i,j} + APC_{i,j}\delta p_{i,j} = 0,$$

$$(BN_{i,j} - BC_{i,j})\delta V_{i,j} + BPC_{i,j}\delta p_{i,j} = 0,$$

$$(CUE_{i,j} - CUC_{i,j})\delta U_{i,j} + (CVN_{i,j} - CVC_{i,j})\delta V_{i,j} = \tilde{T}_{i,j}.$$

Here

$$\tilde{T}_{i,j} = T_{i,j} - (CUE_{i,j}U_{i+1,j} + CUC_{i,j}U_{i,j} + CVN_{i,j}V_{i,j+1} + CVC_{i,j}V_{i,j}).$$

Letting

$$\bar{\beta} = \frac{\delta U_{i,j}}{\delta V_{i,j}} = \frac{(BN_{i,j} - BC_{i,j})APC_{i,j}}{(AE_{i,j} - AC_{i,j})BPC_{i,j}}$$

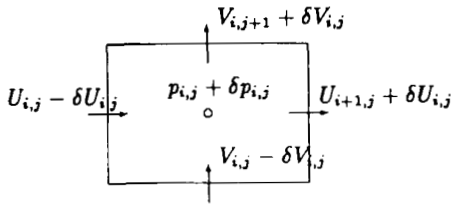

Figure 7. Distributive relaxation schematic

then

$$\delta V_{i,j} = \frac{\tilde{T}_{i,j}}{(CUE_{i,j} - CUC_{i,j})\bar{\beta} + (CVN_{i,j} - CVC_{i,j})}, \qquad \delta U_{i,j} = \bar{\beta}\delta V_{i,j},$$

$$\delta p_{i,j} = \frac{AC_{i,j} - AE_{i,j}}{APC_{i,j}}\,\delta U_{i,j}.$$

Relaxation methods are generally much too slow by themselves to solve the large systems generated at each time step. To obtain optimal efficiency, we therefore use a multigrid method based on this distributive relaxation scheme. A full approximation multigrid scheme (FAS) is used to accommodate non-linearities. A two-level FAS algorithm for an equation of the form

$$L_h u_h = f_h$$

may be described loosely as follows.

1. Relax on $L_h u_h = f_h$.
2. Solve $L_{2h}u_{2h} = L_{2h}I_h^{2h}u_h + \tilde{I}_h^{2h}(f_h - L_h u_h)$.
3. Replace $u_h \leftarrow u_h + I_{2h}^h(u_{2h} - I_h^{2h}u_h)$.

The notation we have introduced includes the difference operators L_h and L_{2h}, the restriction operators I_h^{2h} (for the approximation) and $\tilde{I}_h^{2h}$ (for the residual) and the interpolation operator I_{2h}^h. For details see Reference 5.

6. COMPUTATIONAL RESULTS AND CONCLUSIONS

6.1. Flow transition in a smooth planar channel

To study transition, we considered the least stable eigenmode of the linear theory. For such a mode the linear stability theory provides an approximate analytic solution (which is accurate for small disturbances) to the governing equations (9)–(11) given by

$$u = \varepsilon \mathrm{Real}\{\phi^u(y)e^{i\alpha x - i\omega t}\}, \qquad v = \varepsilon \mathrm{Real}\{\phi^v(y)e^{i\alpha x - i\omega t}\}, \tag{35}$$

where ε is a small positive number and 'Real' stands for 'the real part of'. The complex function $\phi = \phi_R + i\phi_I$ and complex frequency $\omega = \omega_R + i\omega_I$ come from the solution of the Orr–Sommerfeld eigenvalue problem. The Orr–Sommerfeld equation that governs the linear stability of parallel shear flow is

$$\left\{\left(\frac{\mathrm{d}^2}{\mathrm{d}y^2} - \alpha^2\right)^2 - iRe\left[(\alpha u_0 - \omega)\left(\frac{\mathrm{d}^2}{\mathrm{d}y^2} - \alpha^2\right) - \alpha u_0''\right]\right\}\phi = 0,$$

$$\phi(x, 0) = \phi(x, 2) = \phi'(x, 0) = \phi'(x, 2) = 0. \tag{36}$$

The particular problems chosen here for study used $Re = 7500$ and $\alpha = 1$. Equation (36) was solved by a spectral method with Chebyshev polynomials of order 50. The only observed growing mode is characterized by $\omega = \omega_R + i\omega_I$, where $\omega_R = 0{\cdot}24989154$ and $\omega_I = 0{\cdot}00223497$. Note that the streamfunction is given by

$$\psi = \phi(y)e^{i(\alpha x - \omega_R t)},$$

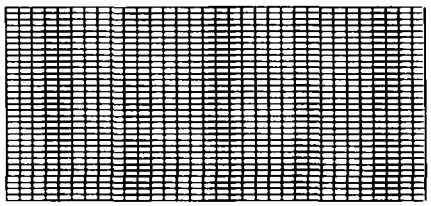

Figure 8. Uniform grid (mesh A)

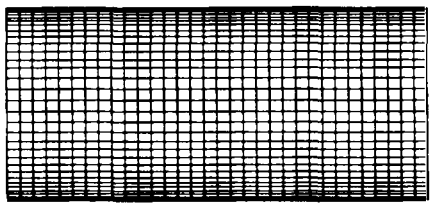

Figure 9. y-direction stretched grid (mesh B)

so the streamwise and normal disturbance velocities can be obtained according to

$$u = \text{Real}\{\phi'(y)e^{i(\alpha x - \omega_R t)}\}, \qquad v = \text{Real}\{-i\phi(y)e^{i(\alpha x - \omega_R t)}\}.$$

Setting $\alpha = 1$, we obtain the eigenfunctions for both u and v in the following forms:

$$\phi^u(y) = \phi^u_R + i\phi^u_I = \phi'(y), \qquad \phi^v(y) = \phi^v_R + i\phi^v_I = -i\phi(y). \tag{37}$$

The initial disturbance is chosen from (35) at $t = 0$:

$$u^0 = \varepsilon(\phi^u_R \cos x - \phi^u_I \sin x), \qquad v^0 = \varepsilon(\phi^v_R \cos x - \phi^v_I \sin x), \tag{38}$$

where ε is set to 0·0001.

We used a time step $\Delta t = T_0/500 = (2\pi/\omega_R)/500$ and studied the behaviour of the simulation on a uniform grid (mesh A of Figure 8) for verification and a y-direction stretched grid (mesh B of Figure 9) to test our transformation scheme. Both meshes are 34 × 130. For mesh B the spacing in the x-direction is uniform but the spacing in the y-direction is such that the grid becomes finer near the solid walls.

We compared the results obtained from our numerical scheme against (35), which is the analytic solution for a small disturbance. For these comparisons we observed the disturbance kinetic energy

$$E = \frac{1}{2}\int_0^2 dy \int_0^L (u^2 + v^2)\, dx. \tag{39}$$

For sufficiently low-amplitude waves this should exhibit exponential behaviour:

$$E(t) = E_0 e^{2\omega_I t} \quad \text{or} \quad \log[E(t)/E_0] = 2\omega_I t, \tag{40}$$

where E_0 is the disturbance energy at $t = 0$.

The computational results of the perturbation energy distribution are shown in Figure 10(a).

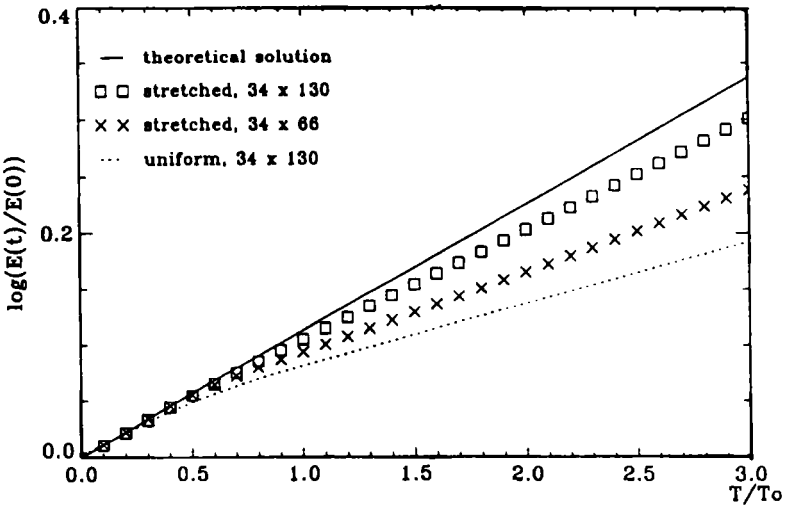

Figure 10(a). Comparison of perturbation energy distributions obtained on different grids during three T-S periods for $Re = 7500$

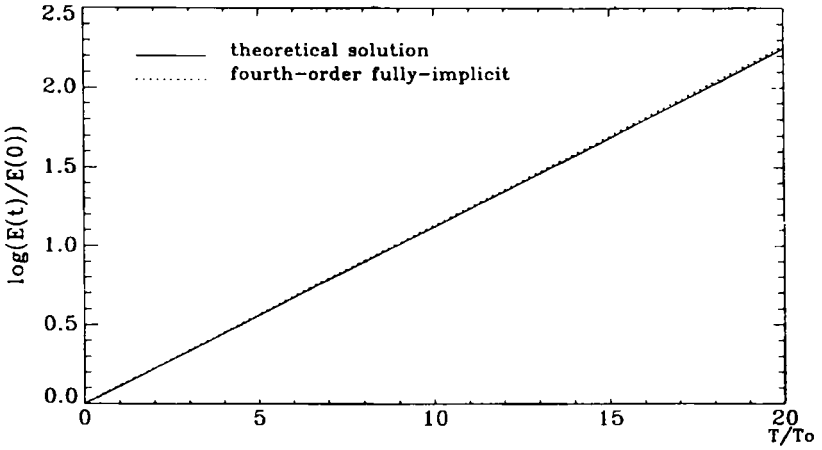

Figure 10(b). Comparison of perturbation energy distributions obtained by fourth-order scheme (on a 34 × 130 grid) and linear stability theory during 20 T-S periods for $Re = 7500$

It is clear that the results obtained by mesh B are better than those obtained by mesh A. Figure 11 depicts the streamfunction contours at selected time steps, showing that the amplitude of the disturbance grows with time, as expected, and that the phase accuracy (travelling wave speed) is very good. Although the spectral method can get more accurate results, the current approach is more suitable for general geometric boundaries. On the other hand, the accuracy of the results become much better when we use the fourth-order scheme (see Figure 10(b)).

6.2. Flow transition in a channel with one and two roughness elements

To study the affect of boundary roughness elements on transition, we used the original Navier–Stokes system (1)–(3) as the governing equations. Note that this is a spatially evolving

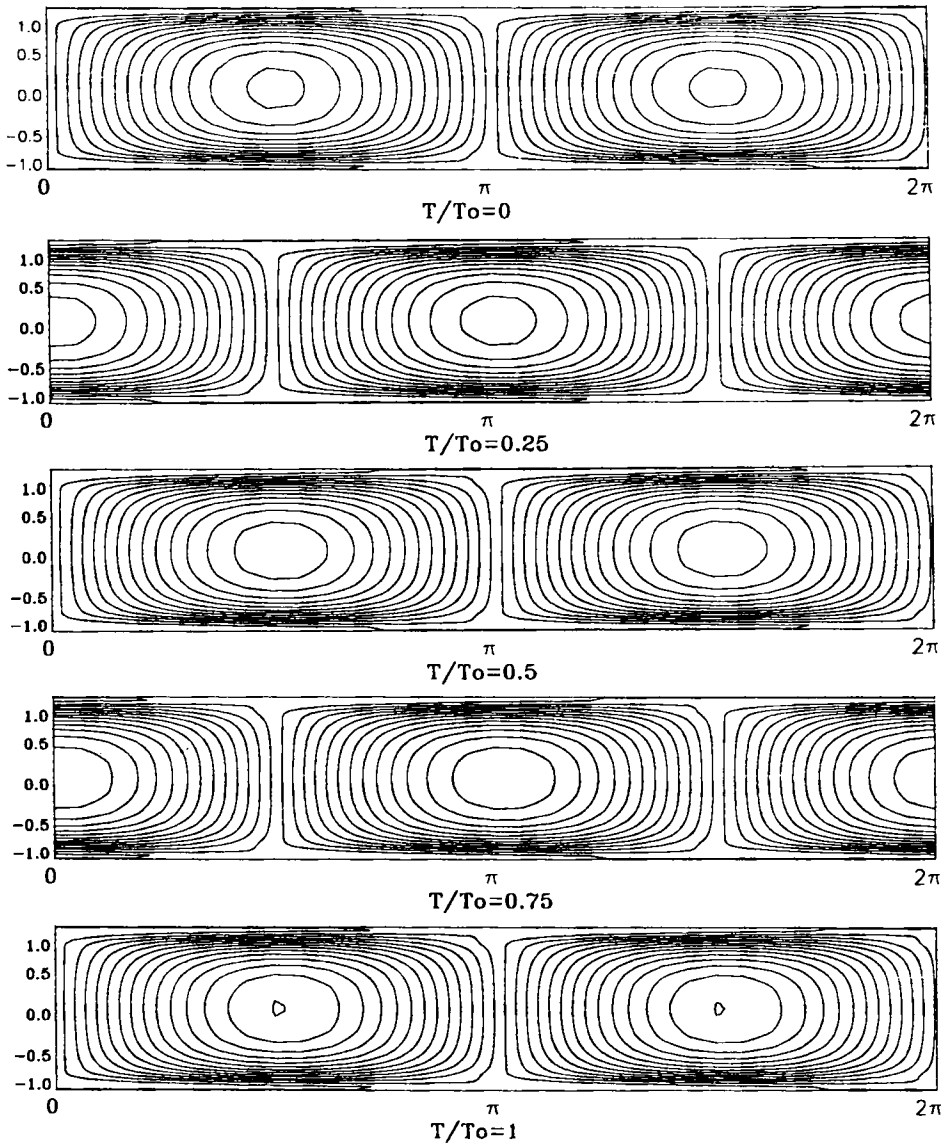

Figure 11. Contour plots of perturbation streamfunctions at selected times for $Re = 7500$. Grid 34 × 130; flow direction is from left to right

instability problem. Letting $Re = 5000$ and $\omega = 0{\cdot}33017$, we then obtained $\alpha_R = 1{\cdot}1557$ and $\alpha_I = 0{\cdot}0106$ from the Orr–Sommerfeld equation (36), which specifies a damping mode. Figure 12 shows the computational domains used in our tests.

We used the same approach described above to solve equations (1)–(3), with the difference here that we need to solve equations (1)–(3) first to obtain the base flow. The computational domain is set to six T-S wavelengths (five wavelengths physical domain and one wavelength buffer domain) and the grid size is 170 × 50. The grid is slightly stretched so that there are more grid points in the recirculation zone. To maintain the high accuracy needed for transition

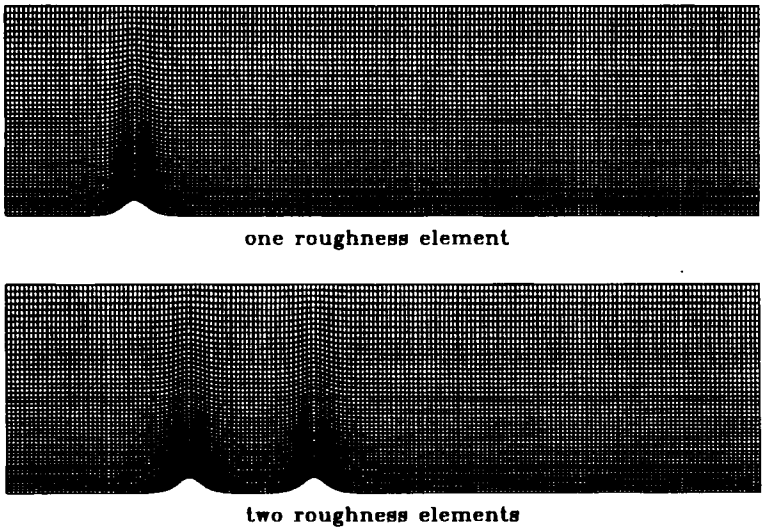

Figure 12. Grids for the rough channel with single and double roughness elements

simulation, an analytical mapping is used here to eliminate additional errors induced by the numerical scheme. The height of the hump is set to $\kappa = 0{\cdot}15$ and the shape of the lower solid wall is given by

$$y_0(x) = \kappa \sum_{n=1}^{m} \operatorname{sech}^2[\sqrt{2}(x - x_{ipn})]. \tag{41}$$

For the one-hump case $m = 1$ and $ip1 = 28$; for the two-hump case $m = 2$, $ip1 = 42$ and $ip2 = 70$. For these two special cases we used the solution obtained at time $t = 95{\cdot}15$ as the base flow. Based on this, we then imposed a disturbance at the flow inlet with amplitude $\varepsilon = 0{\cdot}0025\sqrt{2}$. The contours of the streamfunction for this disturbance are illustrated in Figure 13.

To study the effect of roughness on flow transition, a Fourier transformation was applied to analyse the computational results. This allowed us to determined the distribution of various Fourier modes. Note that

$$\bar{u}(x, y, k) = \frac{\omega}{2\pi} \int_t^{t+T} \tilde{u}(x, y, t) e^{ik\omega t}\, \mathrm{d}t, \tag{42}$$

where $\tilde{u}(x, y, t)$ is the complex disturbance velocity and $\bar{u}(x, y, k)$ is the Fourier coefficient associated with the frequency $k\omega$ at point (x, y). Then

$$|\bar{u}(x, y, k)| = 2\sqrt{[a(x, y, k)^2 + b(x, y, k)^2]} \quad k = 0, 1, 2, \ldots, \tag{43}$$

with

$$a(x, y, k) = \frac{\omega}{2\pi} \int_t^{t+T} \mathrm{Real}\{\tilde{u}(x, y, t)\}\cos(k\omega t)\mathrm{d}t,$$

$$b(x, y, k) = \frac{\omega}{2\pi} \int_t^{t+T} \mathrm{Real}\{\tilde{u}(x, y, t)\sin(k\omega t)\mathrm{d}t. \tag{44}$$

It is well known that only the fundamental wave ($k = 1$) exists for smooth channel flow at

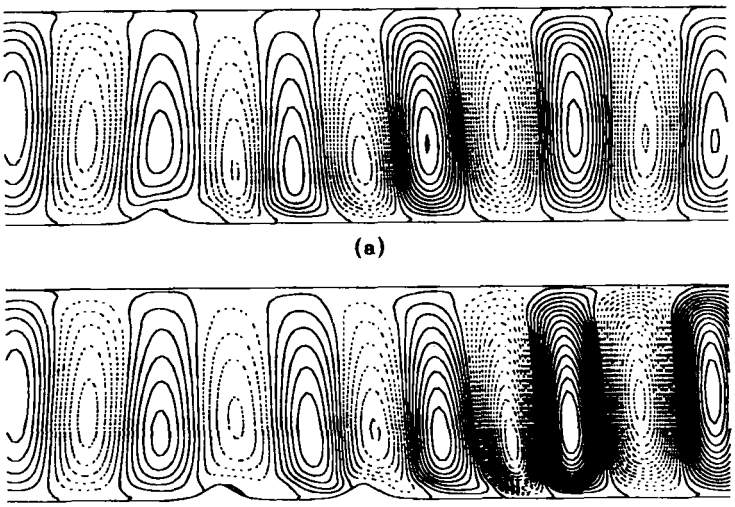

Figure 13. Streamfunction contours for (a) single roughness and (b) double roughness obtained at $t = 6T$ on a 170 × 50 grid. $Re = 5000$, $\varepsilon = 0{\cdot}0025\sqrt{2}$ and $\kappa_l = 0{\cdot}15$. Dashed lines indicate negative contours and flow direction is from left to right

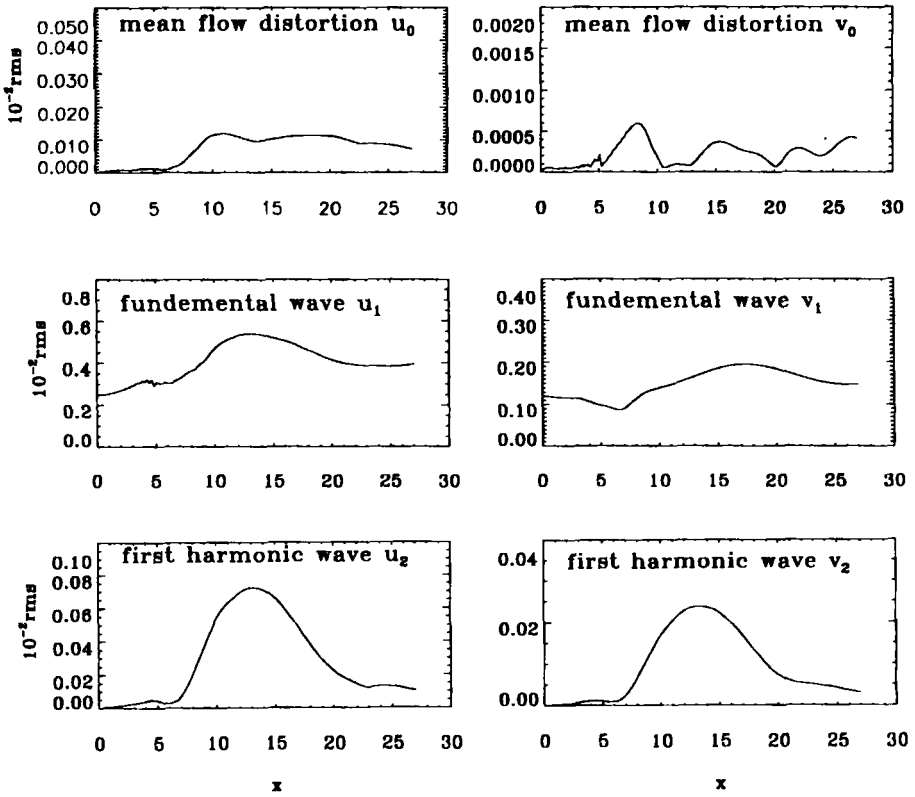

Figure 14. Maximum amplitudes of fundamental wave u_1, v_1, mean flow distortion u_0, v_0 and first-harmonic wave u_2, v_2 for $Re = 5000$, $\kappa_l = 0{\cdot}15$ and $\varepsilon = 0{\cdot}0025\sqrt{2}$ with one roughness element (grid 170 × 50)

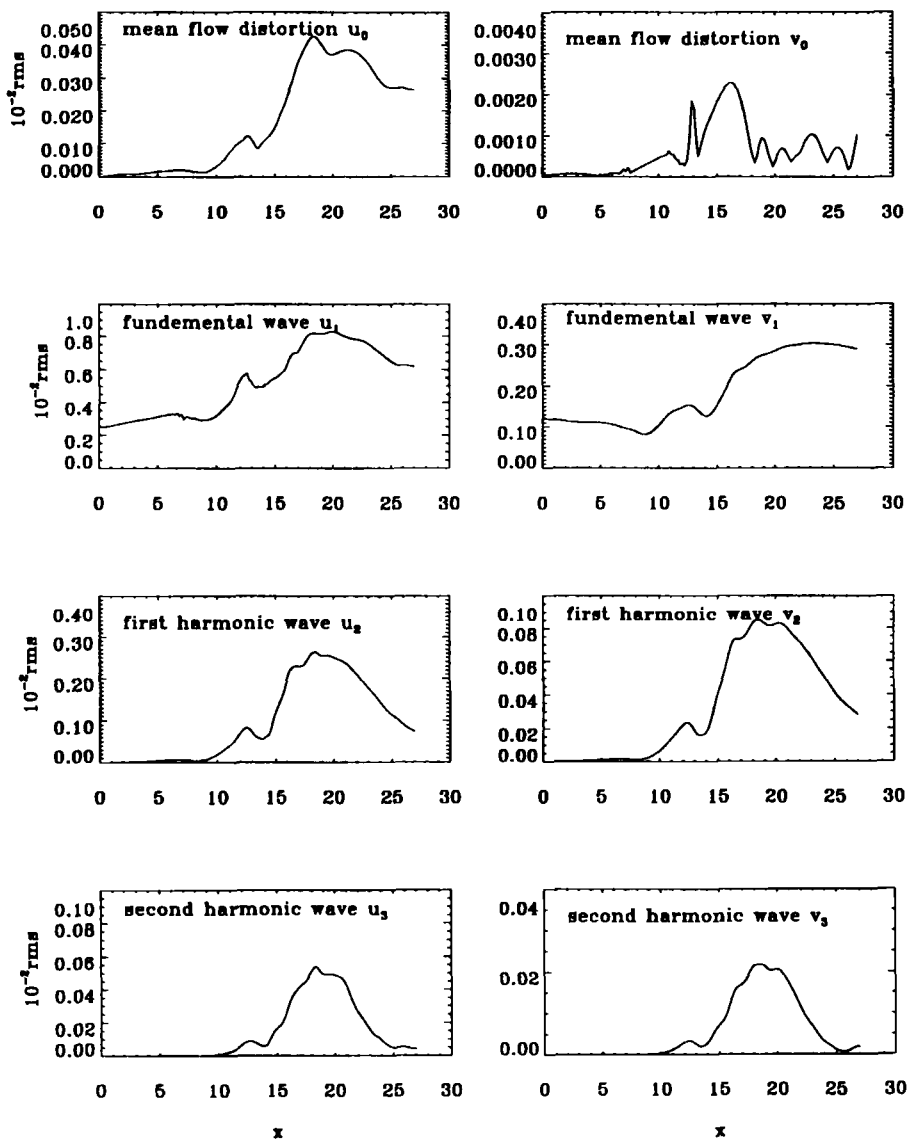

Figure 15. Maximum amplitudes of fundamental wave u_1, v_1, mean flow distortion u_0, v_0, first-harmonic wave u_2, v_2 and second-harmonic wave u_3, v_3 for $Re = 5000$, $\kappa_l = 0{\cdot}15$ and $\varepsilon = 0{\cdot}0025\sqrt{2}$ with two roughness elements (grid 170 × 50)

the stage of linear evolution. However, several Fourier components were obtained for channel flow with roughness elements. Figures 14 and 15 depict the maximum amplitudes of the mean flow distortion u_0, v_0, the fundamental wave u_1, v_1, and the first-harmonic wave u_2, v_2, for the channels with one and two humps respectively.

While few numerical or experimental results exist with which to compare our computational results, what we have obtained does seem at least qualitatively reasonable. According to linear stability theory, when the Reynolds number is not high enough, say $Re = 5000$, the flow in a

planar channel is stable. Because of the influence of roughness elements, the flow becomes unstable, which can be seen clearly from Figures 13–15. In Figure 13 the disturbance waves are obviously increasing for some distance after the hump. Figures 14 and 15 show that in channels with one or two roughness elements, not only the increasing rate of the fundamental wave changed, but also the mean flow distortion and the first-harmonic wave appeared. This suggests that transition will appear earlier in a rough channel than it will for a smooth one.

Since this study only concerns the 2D case, it is impossible to observe more evidence of flow transition to turbulent, but clearly the stability of laminar flow becomes worse in the rough channels.

6.3. Conclusions

Based on the above computations, we conclude the following.

1. Grids that respond to boundary layers and irregular domains can achieve the same accuracy with significantly fewer grid points than a uniform grid.
2. Co-ordinate transformations can be used so that the computational continuity equation maintains its conventional form, which enables easy application of a simple distributive relaxation scheme and an efficient multigrid method to solve the discretized system at each time step.
3. In the computational plane the grids are still uniform, which is convenient for high-order discretization and standard multigrid implementation.
4. The code based on our method can be used for efficient solution of flow problems with fairly general geometries, including e.g. transitional flow in a channel with roughness elements.

ACKNOWLEDGEMENT

This work was supported by NASA under grant NAS1-19312. The authors thank Drs Tom Zang, Craig Streett and Ron Joslin at NASA Langley Research Center and Dr. Helen Reed at Arizona State University for their experienced guidance and helpful discussions.

REFERENCES

1. J.-P. Zahn, J. Toomre, E. A. Spiegel and D. O. Gough, 'Nonlinear cellular motions in Poiseuille channel flow', *J. Fluid Mech.*, **64**, 319–345 (1974).
2. S. A. Orszag and A. T. Patera, 'Subcritical transition to turbulence in plane channel flows', *Phys. Rev. Lett.*, **45**, 989–993 (1980).
3. T. A. Zang and M. Y. Hussaini, 'On spectral multigrid methods for the time-dependent Navier–Stokes equations', *Appl. Math. Comput.*, **19**, 359–372 (1986).
4. L. Kleiser and T. A. Zang, 'Numerical simulation of transition in wall-bounded shear flows', *Ann. Rev. Fluid Mech.*, **23**, 495–537 (1991).
5. C. Liu, Z. Liu and S. McCormick, 'Multigrid methods for flow transition in planar channel', *Comput. Phys. Commun.*, **65**, 188–200 (1991).
6. C. Liu, Z. Liu and S. McCormick, 'Multilevel adaptive methods for incompressible flow in grooved channels', *J. Comput. Appl. Math.*, **38**, 283–295 (1991).
7. Z. Liu, C. Liu and S. McCormick, 'High-order finite difference and multigrid methods for flow transition in a planar channel', *Proc. 4th Int. Symp. on CFD*, 1991, Vol. II, pp. 705–710, UC-Davis, California (1991).
8. C. L. Streett and M. G. Macaraeg, 'Spectral multi-domain for large-scale fluid dynamics simulations', *Appl. Numer. Math.*, **6**, 123 (1989).
9. C. Liu and Z. Liu, 'High-order finite difference and multigrid methods for spatially-evolving instability', *J. Comput. Phys.*, **106**, 92–100 (1993).